Coupling of a lifting-line and unsteady aerodynamics model with a CFD solver

Daniel Linton*
The University of Sydney, Sydney, New South Wales, 2006, Australia

George Barakos†
University of Glasgow, Glasgow, G12 8QQ, United Kingdom

Ronny Widjaja‡
Defence Science and Technology Group, Melbourne, Victoria, 3207, Australia

Ben Thornber§
The University of Sydney, Sydney, New South Wales, 2006, Australia

Momentum source methods are an efficient means of representing airfoils in Navier-Stokes CFD simulations. Momentum source terms are added to the Navier-Stokes equations instead of resolving the solid boundary of the airfoil with a mesh. These source terms are calculated using an aerodynamics model. This approach is useful where the overall performance and mid- to far-field influence of a wing or rotor are desired and details of the flow field near the blade are not the objective of the simulation. One example is simulation of rotorcraft operations where the objective may be to assess an operation's feasibility in terms of control margins, rather than to inform rotor design decisions. Coupling an aerodynamics model to a CFD solver is straightforward in cases where the airflow relative to the blade is steady. Unsteady conditions require an unsteady aerodynamics model, complicating the coupling with the CFD solver. A coupling method is proposed whereby the incident velocity is extracted from the CFD solution and corrected using a theory based approximation for the unsteady induced velocity. The steady-state momentum source method is demonstrated for 2D and 3D simulations and the unsteady coupling method is validated against experiments on a pitching airfoil and verified for blade-vortex interactions. The unsteady coupling method enables meaningful incident velocities to be extracted from unsteady flow-fields, as shown by agreement with experiments and simulations using analytical expressions for the incident velocity in place of the CFD solver.

Nomenclature

*Postgraduate Student, School of Aeronautical Mechanical and Mechatronic Engineering, AIAA Student Member.
†Professor, School of Engineering, AIAA Member.
‡Science Team Lead, Helicopter Systems Effectiveness, Aerospace Division.
§Associate Professor, School of Aeronautical Mechanical and Mechatronic Engineering, AIAA Member.

A, b	=	unsteady aerodynamics constants	
c	=	chord length	[m]
C_l, C_L	=	2D and 3D lift coefficients	
E	=	Jones' correction factor for the effect of the chord	
$\boldsymbol{F}$	=	specific force (normalised by density)	[m/s^2]
F_L	=	Sectional lift force	[N/m]
g_c, g_n	=	chordwise and chord normal distribution functions	
k	=	turbulent kinetic energy (or non-dimensional pitch rate)	[m^2/s^2]
M	=	Mach number	
p	=	pressure (normalized by density) or coordinate of sample point	[m^2/s^2]
$\boldsymbol{R}$	=	Reynolds stress tensor	
r_c	=	vortex core radius	[m]
Re	=	Reynolds number	
s	=	$2U_\infty t/c$ non-dimensional time	
S	=	span	[m]
$\boldsymbol{S}$	=	momentum source term	[m/s^2]
$\boldsymbol{T}$	=	time constant	
$\boldsymbol{U}$	=	velocity vector	[m/s]
u, v, w	=	velocity components	[m/s]
x, y, z	=	spatial coordinates	[m]
Δx	=	sample point offset	[m]
X, Y, Q, R	=	deficiency functions	
y^+	=	Dimensionless wall distance	
α	=	angle of attack	[rad]
ε	=	Standard deviation of Gaussian distribution	
Γ	=	circulation	[m^2/s]
$\hat{\Gamma}$	=	Γ/cU_∞ non-dimensional circulation	
λ	=	downwash velocity	[m/s]
ν, ν_t	=	kinematic viscosity, turbulent viscosity	[m^2/s]
ω	=	specific energy dissipation rate (or angular velocity)	[1/s]

Subscripts

c	=	spatial coordinate normalized by chord length

eff = effective value

in = induced velocity

n = timestep

∞ = freestream or pseudo-freestream velocity

Introduction

Fully-resolved Navier-Stokes simulations of wings and rotor blades have been established as a means of predicting aerodynamics in both steady and unsteady conditions for most regions of the operational envelope[1, 2]. Provided the expertise, appropriate validation, and the computational resources these simulations can produce accurate predictions of performance, though challenges remain for analysis of complex configurations[3] and prediction of sensitive parameters such as rotor figure of merit[4]. One of the great advantages of Navier-Stokes simulations is the ability to compute the flow-field around arbitrary geometries. Aerodynamic interactions between these geometries are naturally captured as a consequence of the solution method and complete information about the flow-field may be obtained. Other simulation and modelling methods which are less computationally expensive are also available, these include lifting line and lifting surface representations of the wing/blade with singularity-based vortex models of the wake, and, in the case of rotors, momentum theory methods[5]. These methods can quickly provide good performance predictions but are formulated for the aerodynamics of wings and rotors and cannot be used alone for domains containing arbitrary geometries and flow features such as bluff bodies and atmospheric boundary layers.

In certain scenarios the performance of a rotor or wing is strongly dependent on interactions with a flow-field generated by both aerodynamic and non-aerodynamic bodies. Examples of such scenarios include wind turbine farms in which the individual turbine wakes interact with one another and with the flow over the surrounding terrain[6, 7], and concurrent rotorcraft operations from a flight deck in which the interaction between rotor wakes and the wake generated by the superstructure and deck of the ship impact handling and performance[8]. The range of geometries and the importance of aerodynamic interactions between separated bluff-body wakes and rotor wakes in these cases suggest the use of Navier-Stokes simulation to compute the flow-field. The examples given are also by their nature large simulations with multiple rotors - making Navier-Stokes simulation a costly option. Compounding this issue is the need to compute variations of these simulations with different wind velocities and different configurations of rotorcraft or wind turbines.

If the purpose of these simulations is not to obtain detailed information about the local aerodynamics of the rotor or wing in question, but rather to investigate the overall performance parameters such as loading distributions, thrust, and power, then complete resolution of the airfoil surfaces may not be necessary and the rotor or wing geometry may be replaced by source terms in the Navier-Stokes equations. An appropriate model must be selected to compute these source terms and by extension the loading of the rotor or wing. If the influence of the complex flow-field on the rotor or

wing is to be accounted for then the model must also extract information from the local CFD generated flow-field to enforce two-way coupling.

The objective of this approach is to retain the advantage of Navier-Stokes simulation for the computation of arbitrary aerodynamic interactions while reducing the cost of such simulations to a level that makes them a viable tool for performing parameter sweeps in complex scenarios. This cost reduction is in terms of both computational time (through a decrease in the number of points in the solution, a decrease in the convergence time, and an increase in the time-step size) and pre-processing time (by reducing the complexity of the mesh).

The choice of aerodynamic model and coupling method will determine the predictions that can be made from a coupled simulation and their accuracy. A simpler choice of model for a rotor such as an actuator disc or one based on blade-element momentum theory[9] will produce predictions in a time-averaged sense and impose limitations inherited from the assumptions upon which these models are based. Aerodynamic models which represent individual blades or a wing, such as an actuator line[10] or an actuator blade/surface[11, 12] model, have the ability to capture the response to unsteady flow. However, it is not enough to simply represent individual blades, a sub-model must also be applied to calculate the appropriate response to the time-varying CFD flow-field.

In this paper an aerodynamics model based on a lifting line representation of a wing and its wake is combined with an unsteady aerodynamics sub-model and coupled to a CFD solver. Unsteady aerodynamic effects on the coupling between the airfoil-generated vorticity and the velocity sampled ahead of the airfoil is demonstrated in this paper and a new unsteady aerodynamics model is proposed to account for these effects. This work builds on previous actuator surface models which implement dynamic stall models, such as the actuator surface model of Shen et al.[11]. Detailed analysis of tip vortex formation and convection behind a wing simulated using this method is also presented.

The test cases presented here show validation of the coupled solver for steady-state cases in 2D and 3D as well as 2D blade-vortex interaction (BVI) and a 2D pitching airfoil. These cases show that the coupled solver is able to reproduce realistic loading in both steady and unsteady flow and that the underlying method is suitable for extension to the simulation of complete rotors in complex operating environments.

Numerical Methods

The numerical methods applied in this study are separated into three distinct components: the Navier-Stokes solver used to compute the flow-field, the aerodynamics model for the calculation of blade loading, and the coupling algorithm joining the two.

Navier-Stokes Solver

The OpenFOAM CFD code was used for all simulations in this work. OpenFOAM is an open-source CFD code composed of a set of libraries and applications for the numerical solution of the equations of fluid dynamics using the

finite volume method. Two different solvers from the OpenFOAM suite were used for the simulations presented here - an unsteady incompressible solver, and a steady-state incompressible solver.

The unsteady solver applies the PISO algorithm[13] to resolve the coupling between the velocity and pressure fields in the incompressible Reynolds-averaged Navier-Stokes equations (Eq. (1) and (2)), while the steady solver uses the SIMPLEC algorithm[14]. All simulations were performed using the $k-\omega$ SST turbulence model[15].

$$\frac{\mathrm{d}\bar{\boldsymbol{U}}}{\mathrm{d}t} + (\bar{\boldsymbol{U}} \cdot \nabla)\bar{\boldsymbol{U}} + \nabla \cdot \boldsymbol{R} = -\nabla\bar{p} + \nabla \cdot (\nu\nabla\bar{\boldsymbol{U}}) + \boldsymbol{S} \tag{1}$$

$$\nabla \cdot \bar{\boldsymbol{U}} = 0 \tag{2}$$

In the above equations the velocity has been decomposed into time-averaged and fluctuating components $\boldsymbol{U} = \bar{\boldsymbol{U}} + \boldsymbol{U}'$ and $R = \overline{\boldsymbol{U}' \otimes \boldsymbol{U}'}$ is the Reynolds stress tensor. In the $k-\omega$ SST model the Reynolds stress is modelled as an additional viscosity so that the kinematic viscosity ν in Eq. (1) is replaced by an effective viscosity $\nu_{eff} = \nu + \nu_t$. The turbulent viscosity (ν_t) is a function of the turbulent kinetic energy (k) and specific turbulent energy dissipation rate (ω), which are obtained from a pair of transport equations.

A second order upwind-biased interpolation scheme is applied to convective terms. The exception to this is in the three-dimensional case, where second order centred interpolation is blended with first order upwind interpolation using the limiter of van Leer[16] for convection of the turbulent variables, k and ω. Centred, linear interpolation is applied to non-convective terms. A second order implicit discretization is used for the time derivative.

Aerodynamic Model

The aerodynamic model used to calculate the source term in Eq. (1) is based on a lifting line representation of the blade with an unsteady aerodynamics model applied to the sectional aerodynamics.

2D Steady Aerodynamics

In a steady two-dimensional case the calculation of $\boldsymbol{S}$ begins by computing an effective angle of attack, α_{eff}, based on $\boldsymbol{U}$ and the induced velocity ($\boldsymbol{U}_{in}$) from a vortex of circulation Γ located at the quarter chord of the airfoil (assuming the bound vorticity to be concentrated as a line at the quarter chord). This effective angle of attack is correlated to a load ($\boldsymbol{F}$) via a table of aerodynamic coefficients for the particular airfoil geometry. The bound circulation (Γ) corresponding to this load is calculated as a result of the Kutta-Joukowski theorem, $\Gamma = -F_L/U_\infty$. Here, F_L is the lift component of the force per unit span on the airfoil, normalized by density. The bound circulation is stored as the state of the 2D steady model.

The momentum source field is calculated from $\boldsymbol{F}$ according to Eq. (3), (4) (from Kim et al. [17]), and (5).

$$\boldsymbol{S} = g_c(x_c) g_n(y_c) \boldsymbol{F} \tag{3}$$

$$g_c(x_c) = \begin{cases} 0.4 + (3.04/0.25)x_c, & \text{if } 0 \le x_c < 0.25 \\ 3.44 - (3.2/0.25)(x_c - 0.25), & \text{if } 0.25 \le x_c < 0.5 \\ 0.24 - (0.24/0.5)(x_c - 0.5), & \text{if } 0.5 \le x_c \le 1 \\ 0, & \text{otherwise} \end{cases} \tag{4}$$

$$g_n(y_c) = \begin{cases} \frac{1}{c\varepsilon\sqrt{2\pi}} \exp\left(-\frac{1}{2}\left(\frac{y_c}{\varepsilon}\right)^2\right), & \text{if } -3\varepsilon \le y_c \le 3\varepsilon \\ 0, & \text{otherwise} \end{cases} \tag{5}$$

In Eq. (3) the functions $g_c(x_c)$ and $g_n(y_c)$ are the chordwise and chord-normal source distributions where x_c and y_c are the chord-normalized chordwise and normal coordinates. The distribution defined for g_c in Eq. (4) is a rough approximation of the loading distribution over an airfoil as used by Kim et al.[17]. The truncated Gaussian distribution defined in Eq. (5) smooths the distribution of source terms in the direction normal to the blade to improve the convergence of the CFD solver. The parameter ε in Eq. (5) is the standard deviation of the distribution and defines the distance in the chord normal direction over which the source terms are applied. A value of $\varepsilon = 0.04$ was used for all simulations. The choice of the ε parameter has been shown to be important on coarser grids than are used in the simulations presented here, Jha et al.[18] specify guidelines for ε in such cases. The distributions are normalized such that:

$$\iint g_c(x_c) g_n(y_c)\, \mathrm{d}x_c \mathrm{d}y_c = \int g_c(x_c)\, \mathrm{d}x_c \int g_n(y_c)\, \mathrm{d}y_c = 1 \tag{6}$$

The chordwise distribution, $g_c(x_c)$, is plotted in Fig. 1 along with the complete distribution, $g(x_c, y_c) = g_c(x_c) g_n(y_c)$, over the cross-section of an airfoil.

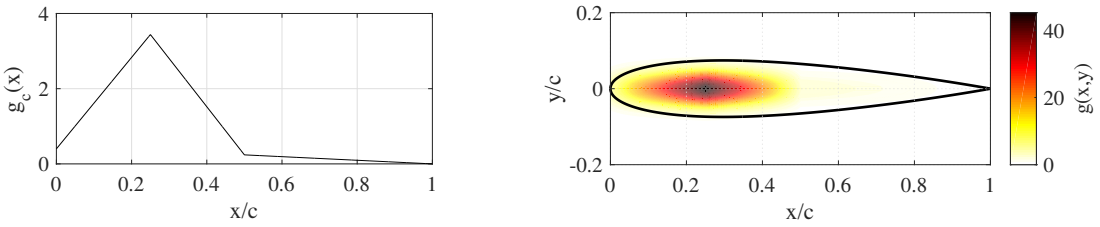

(a) Chordwise distribution function **(b) Product of chord and normal distribution functions**

Fig. 1 2D distribution functions for source terms

The key in this model is the method of obtaining an effective angle of attack. The method used is similar to that of Shen et al.[19] For the case of a 2D airfoil in steady flow this is straightforward: the velocity field may be sampled at a point p, and provided the point is sufficiently far from the airfoil that approximation of the airfoil as a single vortex is valid, then the freestream velocity ($\boldsymbol{U}_\infty$) and effective angle of attack may be retrieved from Eq. (7) and (8). The distance that constitutes "sufficiently far" can be defined as the distance at which the effective angle of attack is no longer dependent on the sample location.

$$\boldsymbol{U}_\infty = \boldsymbol{U}(p) - \boldsymbol{U}_{in}(p) \tag{7}$$

$$\alpha_{eff} = \text{atan}\left(\frac{U_{\infty,n}}{U_{\infty,c}}\right) \tag{8}$$

where $U_{\infty,c}$ and $U_{\infty,n}$ are the chordwise and normal components of the freestream velocity.

2D Unsteady Aerodynamics

Several factors complicate the extension of the calculation of $\boldsymbol{S}$ to cases in which the incident flow is no longer steady and/or the airfoil is accelerating. Firstly, the effective angle of attack can no longer be made independent of the location of the sample point. Consider the case of a vortex approaching a symmetric 2D airfoil at zero angle of attack. If the steady approach to sampling the CFD solution is adopted then the velocity that the airfoil sees will correspond to the velocity at the sample point less the induced velocity. Clearly this will depend on the location of the approaching vortex relative to the sample point and therefore a sensible choice of this point must be made. Our approach is to select a sample point that is as close to the airfoil as possible and which lies in the path of the airfoil.

This choice arises from the assumption that the relative velocity of the flow-field is dominated by the velocity of the airfoil itself, which is known. In this way sampling along the path of the airfoil can be considered equivalent to sampling ahead in time. Our assumption about the relative velocity therefore translates directly into the assumption that changes in the velocity field are slow relative to the time required for the blade to traverse the distance from the quarter chord to the sample point. This implies that the closer the sample point can be brought towards the airfoil the less restrictive this assumption becomes. However, the previously stated condition of sufficient distance between the airfoil and the sample point still applies and so a balance must be found.

Sampling ahead of the airfoil requires the introduction of a delay to ensure that the response occurs when the airfoil reaches the sample point and not when the sample is taken. This delay is enforced by storing the sampled velocity field values and interpolating between these stored values using a time delayed by a constant value, $\Delta T = \Delta x / U_\infty$ (where Δx is the distance between the quarter chord point and the sample point). Figure 2 contains a plot of the sampled angle of attack and the delayed angle of attack during a BVI event with a sample offset of $\Delta x = c$. The angle of attack is plotted

against non-dimensional time, $s = 2U_\infty t/c$.

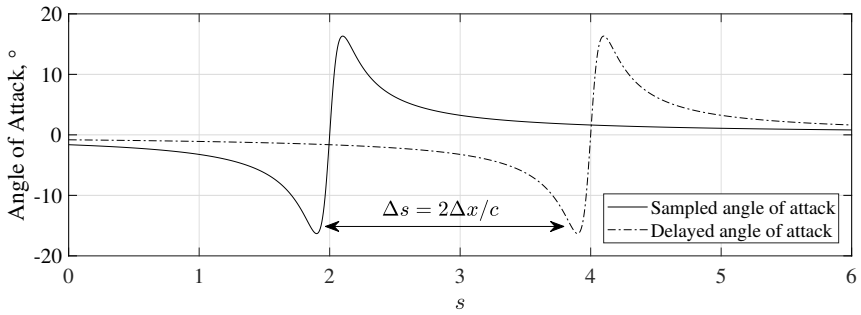

Fig. 2 Sampled and delayed angle of attack during a BVI event.

A second complicating factor is that the response of the airfoil to a time-varying angle of attack displays considerable hysteresis and the simple use of a lookup table is no longer sufficient to predict the loading. To account for this a simple unsteady aerodynamics model which is introduced which reproduces the time delay in the development of the circulation around the airfoil. This is a discrete time model which approximates the response of the circulatory component of the unsteady lift as an exponential series which may be computed at each timestep storing only the value from the previous timestep. This implementation is taken from the work of Beddoes[20] and is applicable to attached flow conditions, though the impulsive terms have been neglected. The model is summarised in Eq. (9).

$$
\begin{aligned}
C_{Nn} &= C_{N\alpha}(\alpha_n - X_n - Y_n) \\
X_n &= X_{n-1}\exp(-\Delta t/T_1) + A_1(\alpha_n - \alpha_{n-1})\exp(-\Delta t/2/T_1) \\
Y_n &= Y_{n-1}\exp(-\Delta t/T_2) + A_2(\alpha_n - \alpha_{n-1})\exp(-\Delta t/2/T_2) \\
T_1 &= [b_1(1-M^2)2U_\infty/c]^{-1} \\
T_2 &= [b_2(1-M^2)2U_\infty/c]^{-1}
\end{aligned}
\tag{9}
$$

where the subscripts n and $(n-1)$ indicate the current and previous timesteps, C_N is the normal force coefficient, α is the quasi-steady angle of attack at the three-quarter chord, X and Y are deficiency functions, and T_1 and T_2 are the time delay constants. M is the local Mach number. The remaining constants A_1, A_2, b_1, and b_2, may be determined experimentally or approximated using classical linear aerodynamic theory[21]. For all simulations in this paper the following values are used: $A_1 = 0.3$, $A_2 = 0.7$, $b_1 = 0.2$, and $b_2 = 0.65$. The sensitivity of the model to these parameters is discussed by Beddoes[20].

This represents a first approximation for the unsteady aerodynamic response of a 2D airfoil and may be substituted with a more sophisticated model covering dynamic stall and deep stall. The coupling between the CFD solver and the aerodynamics model introduces a requirement for a secondary unsteady aerodynamics model. This secondary model

accounts for the response of the flow-field at the sample point to a change in circulation at the airfoil.

Beddoes' discrete numerical expression for the equivalent angle of attack:

$$\alpha_{E,n} = \alpha_n - X_n - Y_n$$

is an approximation for the superposition of indicial functions by application of Duhamel's integral. The influence of the shed vorticity is captured by the deficiency functions X_n and Y_n. The shed vorticity in the wake influences the downwash at the sample point in the same manner as it influences the effective angle of attack at the airfoil. Therefore, a similar discrete formulation is chosen to compute an effective downwash at the sample point:

$$\begin{aligned}
\lambda_{E,n} &= \lambda_n - Q_n - R_n \\
Q_n &= Q_{n-1} \exp(-\Delta t/T_3) + A_3(\lambda_n - \lambda_{n-1}) \exp(-\Delta t/2/T_3) \\
R_n &= R_{n-1} \exp(-\Delta t/T_4) + A_4(\lambda_n - \lambda_{n-1}) \exp(-\Delta t/2/T_4)
\end{aligned} \tag{10}$$

Equation (10) expresses the downwash at the sample point as the sum of the upwash due to the bound circulation (since $\lambda_n = \Gamma_n/2\pi r$) and the downwash due to the vorticity shed into the wake. At each timestep the downwash due to the shed vorticity increases by an increment proportional to the change in circulation ($(\lambda_n - \lambda_{n-1}) = (\Gamma_n - \Gamma_{n-1})/2\pi r$). The exponential factor in the incrementing terms for Q_n and R_n corrects the half-step lag introduced by the discrete formulation.

The influence of the downwash due to previously shed vorticity decreases as it is convected away from the blade, this is modelled by the exponentially decaying terms in Eq. (10). The time constants, T_3 and T_4, should therefore be expected to be functions of the freestream velocity such that both approach infinity as the freestream velocity approaches zero (a physically meaningless condition in which the theoretical vorticity is not convected away from the airfoil) and of some length scale for appropriate dimensionality. $T_3 = b_3\Delta x/2U_\infty$ and $T_4 = b_4 c/2U_\infty$ are therefore chosen as appropriate first approximations. The length scale of $\Delta x/2$ was found to be the appropriate length for the T_3 constant, while the semi-chord is appropriate for the T_4 constant. The model constants were calibrated against a sinking airfoil case for which the induced velocity at the sample point could be extracted directly from the CFD solution.

This analysis of the unsteady induced velocity at the sample point does not account for compressibility, which is artificially removed by the use of an incompressible CFD solver. The argument for the model in Eq. (10) is partially based on analogy to Beddoes' model. To demonstrate its validity, consider the case of an airfoil initially at zero-lift angle of attack which instantaneously begins to sink at a constant velocity. The effect of this motion on the unsteady aerodynamics model described above is to input a step-change in the angle of attack. In this scenario the actual velocity

perturbation at the sample point can be extracted from the CFD solution and compared to the induced velocity due only to the bound circulation on the airfoil as predicted by Beddoes' model, and to the effective induced velocity defined by Eq. (10). Figure 3 shows this comparison for a range of different angle of attack changes, velocities, sample point offsets, and chord lengths. The base values for these parameters were $\Delta\alpha = 2°$, $U_\infty = 200$ m/s, $\Delta x = 1.0c$, and $c = 0.05$ m. As expected, the response of the induced velocity at the sample point lags the response of the airfoil circulation. With model coefficients $A_3 = 0.85$, $A_4 = 0.15$, $b_3 = 2.8$, and $b_4 = 30$ the induced velocity at the sample point is much better predicted. Figure 3 also demonstrates that the formulations of the model and the time constants correctly account for variations in simulation parameters.

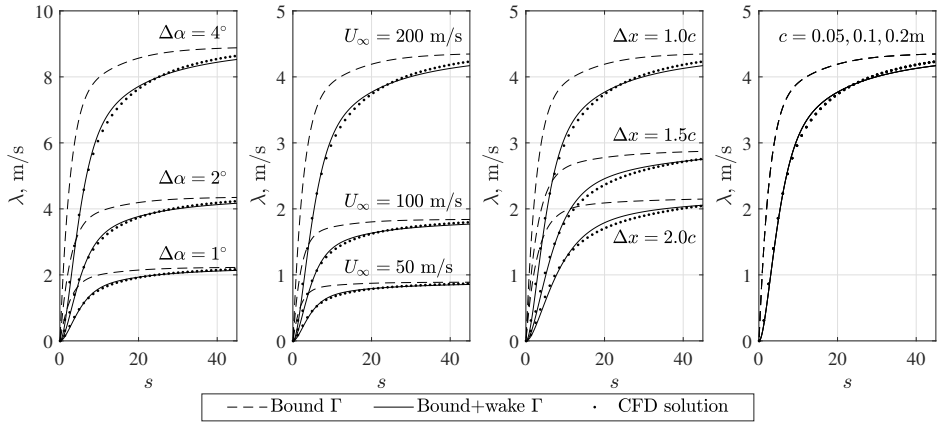

Fig. 3 Response of induced velocity, λ, at sample point.

3D Aerodynamics

A lifting line approximation of a wing is adopted to move from 2D to 3D cases. The wing is divided into spanwise sections, on each of which a bound vortex is placed at the quarter chord. The circulation of each of these bound vortices is calculated by evaluating the 2D model in a plane passing through a collocation point at the midpoint of the vortex.

Unlike the 2D case, there is an additional induced velocity for a finite 3D wing due to the trailed vortices required by Helmholtz's theorems. As a result the induced velocity at the quarter chord point due to the presence of the wing is no longer zero and the sampled velocity must now be converted to an effective velocity according to Eq. (11). This effective velocity is then used to calculate the effective angle of attack at the quarter chord.

$$\begin{aligned} \boldsymbol{U}_\infty &= \boldsymbol{U}_{CFD}(p) - \boldsymbol{U}_{in}(p) \\ \boldsymbol{U}_{eff} &= \boldsymbol{U}_\infty + \boldsymbol{U}_{in}(p_{qc}) \end{aligned} \tag{11}$$

where p_{qc} is the location of the quarter chord point on the section in question.

A wake model must now be introduced in order to evaluate the induced velocity. For the case of a finite wing in steady-state, rectilinear flight the wake model selected is simply comprised of straight, semi-infinite vortex filaments extending in the freestream direction from the edge of each bound vortex. The strength of each trailing vortex is the difference between the strengths of the bound vortices on the adjoining airfoil sections - as per Helmholtz's second theorem. In the case of a rotating wing a more sophisticated model must be used to reflect the complex, helical wake geometry.

Jones' correction for the effect of the chord[22] is applied to the 2D coefficient of lift. This correction scales the coefficient of lift by a factor of $1/E$, where:

$$E = \frac{S + c}{S}$$

for a rectangular planform. This factor approaches one as the aspect ratio tends to infinity.

Coupled Solution Algorithm

Information from the CFD solver is transmitted to the aerodynamics model via the sampling of the velocity field and the output is transmitted back to the CFD solver via the source terms in the momentum equations. The flow-chart in Figure 4 shows how this coupling is incorporated as the first step of the PISO and SIMPLEC algorithms.

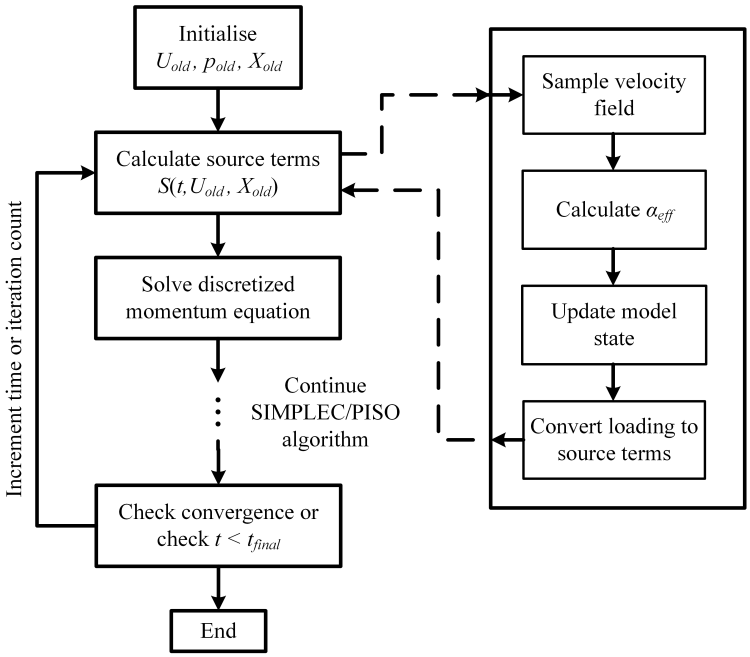

Fig. 4 Flow chart showing the inclusion of the aerodynamics in the solution algorithm.

The first step in the PISO algorithm is the solution of the momentum equation while holding the pressure field fixed

Table 1 Grid independence study for 2D steady airfoil

Cell Count ($\times 10^{-4}$)	0.5	1.9	7.7	30.0
C_l	0.958	1.028	1.039	1.037

at the value from the previous iteration. It is in this step of the algorithm that the momentum source terms are introduced as below.

$$\frac{\mathrm{d}\boldsymbol{U}}{\mathrm{d}t} + (\boldsymbol{U} \cdot \nabla)\boldsymbol{U} - \nu\nabla^2\boldsymbol{U} = -\nabla p + \boldsymbol{S}(t, \boldsymbol{U}, \boldsymbol{K}) \tag{12}$$

The source terms are a function of time, the CFD velocity field, and the model state ($\boldsymbol{K}$) at the previous iteration - as shown in Eq. (12) where values from the previous iteration are denoted with a subscript *old*. The terms on the left-hand side are evaluated using implicit numerical schemes while those on the right are explicit.

Test Cases

Steady 2D Airfoil

Application of the basic momentum source method is first demonstrated for the simple case of a NACA0015 airfoil in steady flow at three different angles of attack: $\alpha = 2°$, $5°$, and $10°$. These simulations were performed on a grid with a fully-resolved airfoil and using the momentum source method. The grids are identical in all respects with the exception that the interior of the airfoil is meshed for the momentum source cases. These simulations were performed with a Reynolds number of 3×10^6.

Grid independence was confirmed by monitoring the coefficient of lift on the resolved airfoil for a set of successively finer meshes. The results of this study and the number of cells in each mesh are contained in Table 1 and the second finest mesh is shown in Fig. 5.

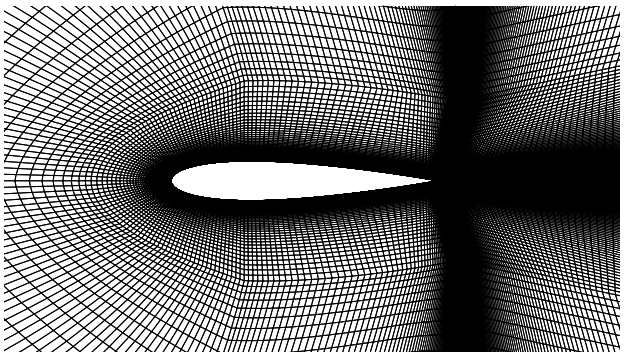

Fig. 5 77k cell grid used for the 2D steady airfoil case

Table 2 Parameters for 2D pitching airfoil simulations

AGARD Test Case	M	α_m (°)	α_0 (°)	k	Re ($\times 10^{-6}$)
CT-1	0.6	2.89	2.41	0.0808	4.8
CT-2	0.6	3.16	4.59	0.0811	4.8
CT-3	0.6	4.86	2.44	0.0810	4.8
CT-5	0.755	0.016	2.51	0.0814	5.5

2D Pitch Oscillation

The first unsteady test case is a 2D airfoil with NACA0012 profile in pitch oscillation. These cases are based on the NACA 0012 Oscillatory and Transient Pitching experiments described in AGARD Report 702[23]. Four of these experiments were replicated with simulations and the Mach number (M), mean angle of attack (α_m), amplitude of the pitching (α_0), reduced frequency ($k = \omega c/2U_\infty$, with ω the pitch frequency), and Reynolds number (Re) of these cases are listed in Table 2. The reduced frequencies of these test cases roughly correspond to between 1/rev and 2/rev pitch oscillations for a blade section on a typical full-scale rotor, depending on the section location. The flow velocities in both this case and the following correspond to Mach numbers of 0.5 and above in standard atmospheric conditions. This is relevant for the unsteady aerodynamics model, which is a function of Mach number, though not for the incompressible CFD solver. Linear compressibility corrections were applied to the aerodynamic coefficients tables.

A circular domain was used for these cases with 40,000 cells and an inlet length of 25 chords. The mesh was refined in the centre of the domain with 60 points along the chord and 10 points across the thickness of the airfoil. This refined region is shown in Fig. 7. To confirm grid independence a refinement study was performed for the CT-1 case. The lift coefficient hysteresis curves from simulations on three different grids are plotted on Fig. 6 and are shown to be independent of the level of refinement.

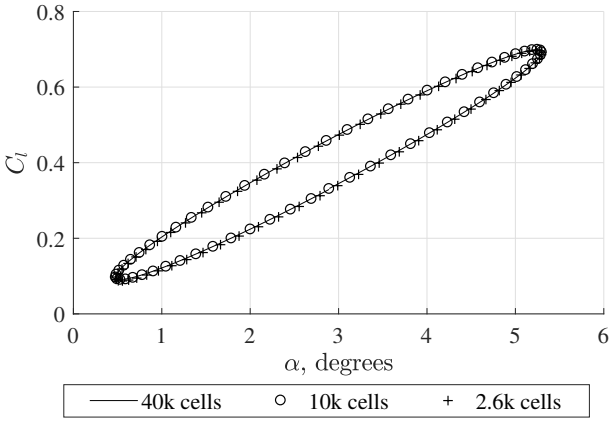

Fig. 6 Lift coefficient hysteresis curve for the AGARD CT-1 test case with three levels of grid refinement.

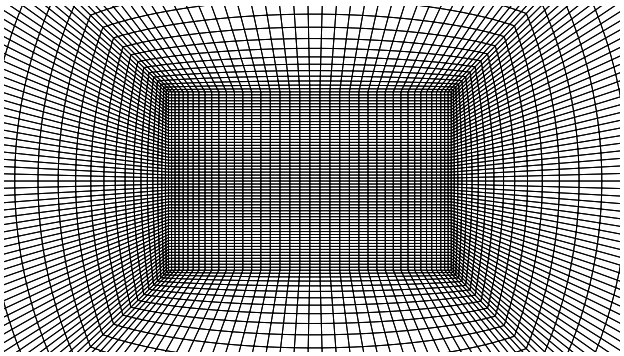

Fig. 7 10k cell grid used for the pitching airfoil case

2D Blade-Vortex Interaction

In most operating conditions the concentrated tip vortices shed from rotor blades are convected away from the rotor disk by the downwash. However, in some circumstances (most notably in low speed descending flight) the rotor will fly through its own wake leading to interactions between tip vortices and rotor blades. These BVI events are responsible for significant rotor noise and vibration.

Figure 8 is an illustration of the tip vortex trajectories from a four-bladed rotor in slow descending flight and shows typical BVI events. The geometry of a BVI event is critical to determining its severity. The angle between the blade and the vortex axis may range between 0° (parallel BVI) and 90° (perpendicular BVI). Two regions for potential BVIs of the perpendicular and parallel kind are annotated in Fig. 8. Parallel BVIs produce the greatest loading variations and generate the loudest sound[24] and the intensity of the response is greatest when the circulation of the vortex is aligned with the bound circulation on the blade, as it would be in the advancing side, parallel BVI shown in Fig. 8. The magnitude of the response also increases with the strength of the vortex circulation and the bound circulation. The closer the vortex passes to the blade, the greater the noise and change in loading - although a direct hit between the leading edge of the blade and the vortex core may result in disruption of the vortex structure and a less violent interaction than a near miss[25].

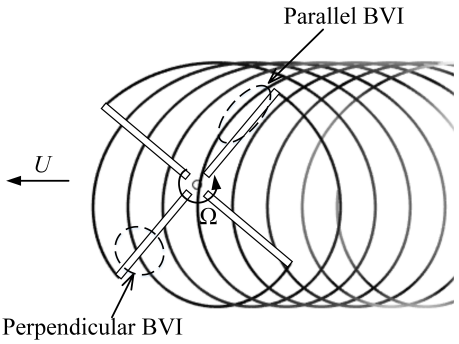

Fig. 8 Overhead view of tip vortex trajectories for a four-bladed rotor in low-speed descent.

Parallel BVI presents a convenient test case as the characteristics of the interaction are two dimensional. A set of head-on 2D BVI simulations were selected to demonstrate the coupling of the unsteady aerodynamics model to the CFD solution. These BVI cases also serve to illustrate the more general case of disturbances convected by the freestream. The airfoil in these simulations is a NACA0012 at 0° angle of attack and a Reynolds number of 3×10^6.

The response of the model was tested for a range of different incident vortices representative of those typically encountered by a rotor. Three different core radii were used, $r_c/c = 0.05$, 0.1, and 0.2. These were each applied to vortices of non-dimensional circulation $\Gamma/cU_\infty = 0.2$ and 0.4 for a total of six cases. The cases were initialised by first producing a steady state solution, then the vortex was introduced 3 chord lengths upstream. The Scully[26] model (Eq. (13)) was chosen to initialise the vortex velocity profile.

$$u_\theta = \frac{\Gamma}{2\pi r}\left(\frac{r^2}{r^2 + r_c^2}\right) \tag{13}$$

The pressure field was initialised by integrating the inviscid equation:

$$\frac{\partial p}{\partial r} = \frac{\rho u_\theta^2}{r} \tag{14}$$

using the velocity profile in Eq. (13). Although this does not represent a valid solution of the viscous, incompressible Navier-Stokes equations (no such solution exists for a steady vortex with no radial velocity component), it was deemed sufficient for introducing a velocity distribution similar to a real vortex that is convected past the momentum source representation of the airfoil by the CFD solver.

The boundaries of the domain for the BVI case were located 100 chord lengths from the airfoil and the purely cartesian grid contained 330,000 cells with refinement along the trajectory of the vortex to ensure at least 10 points within the core radius of the smallest vortex. A schematic of the initialised flow-field with superposed vortex is shown in Fig. 9.

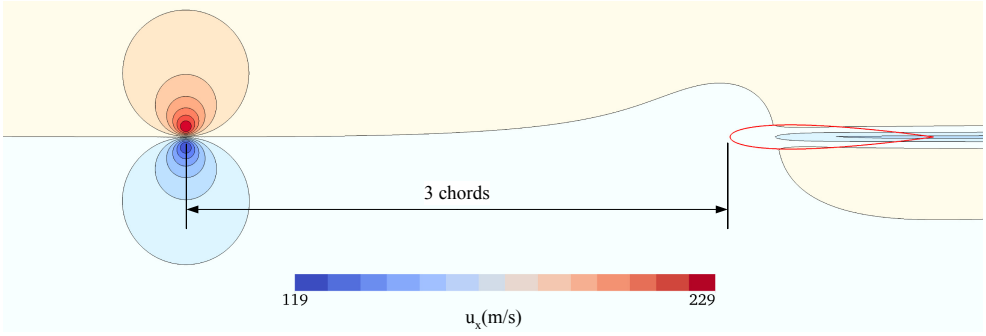

Fig. 9 Contours of x-velocity in the initialised flow-field for a BVI case with vortex parameters: $\hat{\Gamma} = 0.2$ and $r_c = 0.05$.

A grid independence study was conducted to ensure accurate convection of the vortex to the blade. The velocity

profiles across the vortex after convection to the leading edge of the airfoil are plotted in Fig. 10 for three grid refinement levels. The smallest vortex core ($0.05c$) with the greatest circulation ($\hat{\Gamma} = 0.4$) was used for this study.

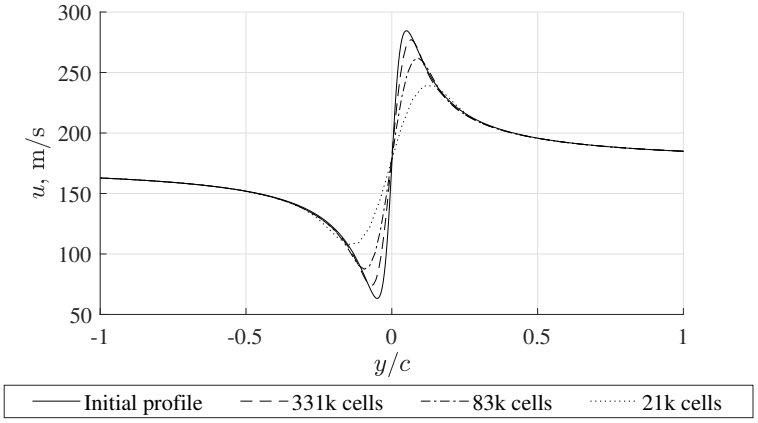

Fig. 10 Vortex velocity profiles after convection on three different grids compared to initial profile.

Steady-State Wing

A wing was simulated at 10° angle of attack in steady flow conditions to demonstrate the application of this method to a 3D case and assess the validity of the wake generated. This case is based on the experiments of Margaris and Gursul[27] and the PIV data from these experiments are used for comparison. The wing has a NACA 0015 profile with an aspect ratio of 5.08 and the experiments were performed at Re $\approx 10^5$ based on freestream velocity and chord length. The locations of the PIV planes in the experiment are shown in Figure 11 along with the coordinate systems used.

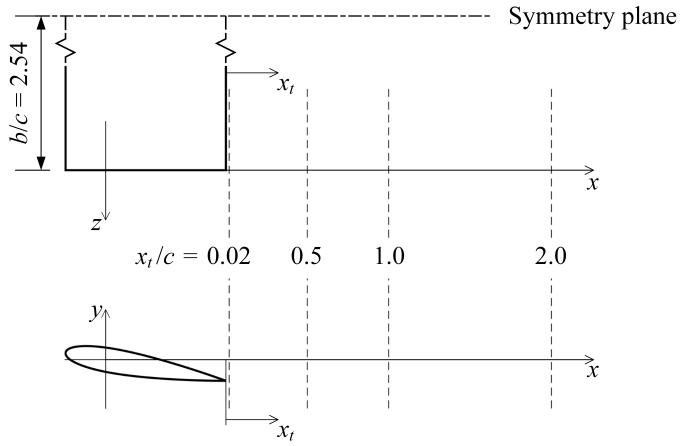

Fig. 11 Location of PIV planes (dashed lines) used by Margaris and Gursul[27] for the finite aspect ratio wing with NACA 0015 profile.

The simulation was performed with a resolved wing and with the coupled method. The size of the domain was

Table 3 Grid independence study for steady-state wing

Cell Count ($\times 10^{-6}$)	0.26	2.04	15.6
C_L	0.605	0.616	0.620

halved by applying a symmetry boundary condition at the mid-span in the resolved simulation. External boundaries were placed 100 chord lengths from the wing in all directions and a C-grid topology was used for the mesh. The resolved simulation was run with 15 million grid points for the half-domain (maximum y^+ of 0.6, average of 0.1) while the coupled simulation used 10 million grid points for the full domain. The mesh around the resolved blade is shown in Fig. 12. A set of 2D precursor simulations were performed to obtain the aerodynamic table data for the 2D aerodynamics model and 61 spanwise panels were used to represent the wing. A cosine distribution was used to cluster the panels towards the wing tips.

Grid independence was confirmed by monitoring the coefficient of lift on the resolved wing for a set of successively finer meshes. The results of this study and the number of cells in each mesh are contained in Table 3.

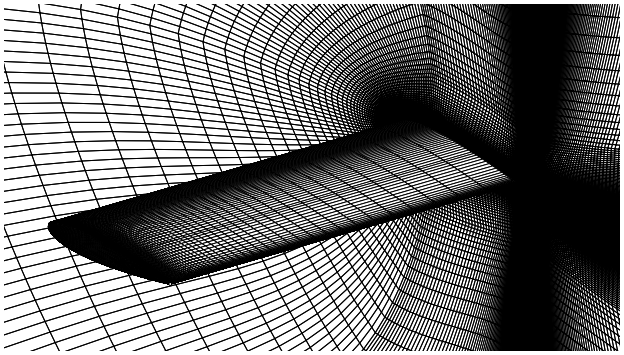

Fig. 12 Fine grid used for the steady-state wing

Results

Steady 2D Airfoil

Streamlines and contours of pressure coefficient around a NACA0015 airfoil are shown in Fig. 13 for three different angles of attack. These results provide a comparison of the local flow-field generated by the momentum source representation of the airfoil with that generated by a resolved airfoil. The most notable difference is in the pressure near the airfoil, particularly at lower angles of attack where the local pressure field isn't dominated by lift generating forces. This highlights one of the limitations of this momentum source method, that is the lack of geometry modelling in the local flow field. It is possible that a more sophisticated model for the distribution of source terms in the mesh would produce a more realistic result in the near-field. More important for the utility of this method are results in the mid- to far-field and the overall streamline curvature. In these regards the momentum source method performs well.

Streamlines show good agreement in Fig. 13 and the pressure fields reach agreement away from the airfoil. Results from the far-field are discussed below for a finite aspect ratio wing.

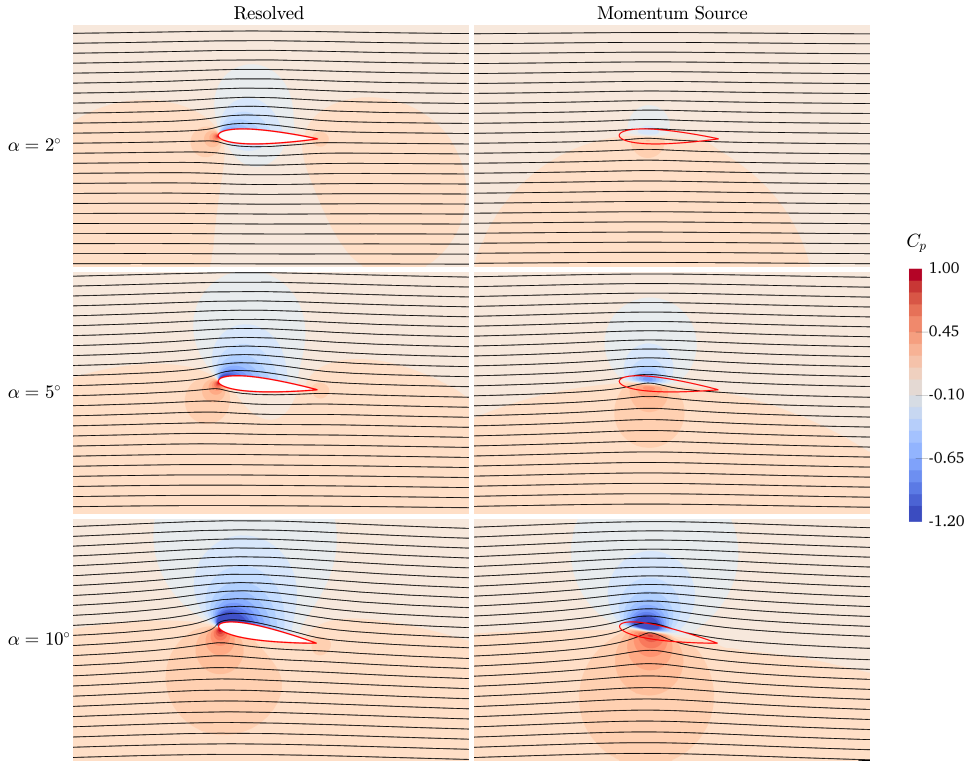

Fig. 13 Comparison of pressure coefficient contours and streamlines around a resolved NACA0015 airfoil and a momentum source representation of the airfoil.

2D Pitch Oscillation

The coefficient of lift is plotted as a function of pitch angle for each of the AGARD test cases in Fig. 14. The experimental results from AGARD Technical Report 702[23] are plotted alongside the results from the unsteady aerodynamics model, both coupled and uncoupled from the CFD solution, as well as without the wake corrections of Eq. (10). The uncoupled results were obtained by using the relative velocity as input to Beddoes' unsteady aerodynamics model. The agreement with the experimental data is good for all four cases and the almost exact alignment of the coupled and uncoupled results demonstrates that the method of coupling to the CFD solver is valid. This implies that the limiting factor in improving the accuracy of loading predictions is the aerodynamics model rather than the coupling method.

The results of the simulations performed without the wake correction are skewed due to the induced velocity correction leading the actual induced velocity in the flow-field. This lead in the velocity correction causes the hysteresis curves to exhibit a shallower mean lift-curve slope than predicted by the uncoupled unsteady aerodynamics model and

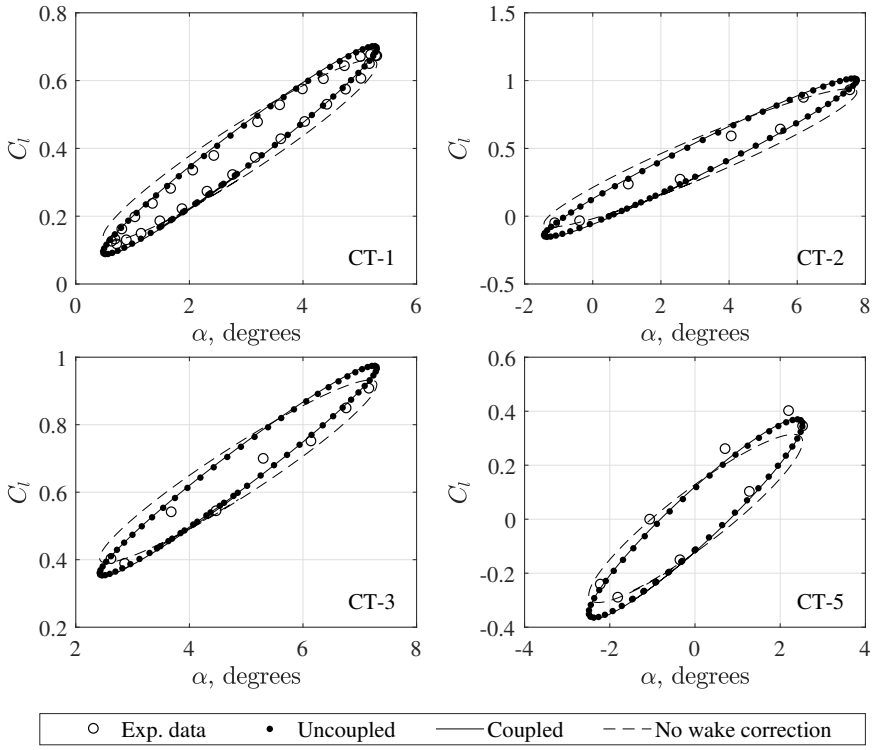

Fig. 14 Lift coefficient vs. angle of attack for a pitching NACA0012 airfoil.

as found in the experimental data. Figure 15 shows the phase lead and over-prediction of the induced velocity at the sample point when using the bound circulation only. The results from the model with the wake correction show almost exact agreement with the sample induced velocity from the CFD solution.

2D Blade-Vortex Interaction

The influences of the unsteady aerodynamics model, the delay function, and the wake correction are shown in Fig. 16. The response of the coupled model without Beddoes' unsteady aerodynamics model and without the wake correction is shown by the dashed line. There is a significant over-prediction of the unsteady lift at impact ($s = 6$) followed by non-physical oscillations at periods corresponding to the delay function. These oscillations are caused by two factors: the over-prediction of the induced velocity correction, and the lead on the correction due to the lack of wake correction. When the vortex initially reaches the airfoil the induced velocity is over-predicted at the sample point and the over-corrected effective velocity is stored by the delay function. Once the delay period has passed this effective velocity reaches the airfoil and the airfoil "sees" an inverse profile of the initial vortex encounter. This repeats until the oscillations have been damped.

The same post-vortex oscillations can be seen in the response of the coupled model with Beddoes' unsteady

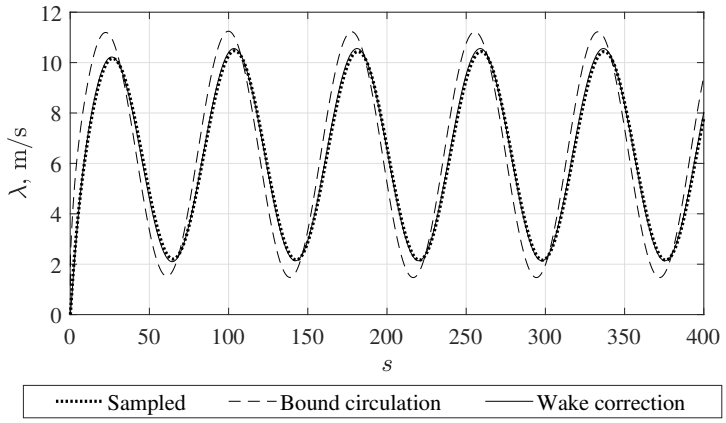

Fig. 15 Induced velocity (λ) at the sample point as a function of non-dimensional time in the AGARD CT-1 test case.

aerodynamics model but without the wake correction (as shown by the dotted line). Here the magnitude of the oscillations are not as large because the initial response is not over-predicted. The purpose of the delay function is illustrated by the dash-dot line which has the same form as the complete model except with a large lead in the response. The complete model exhibits the expected behaviour with the response occurring at the time of impact and no spurious oscillations in the aftermath of the encounter.

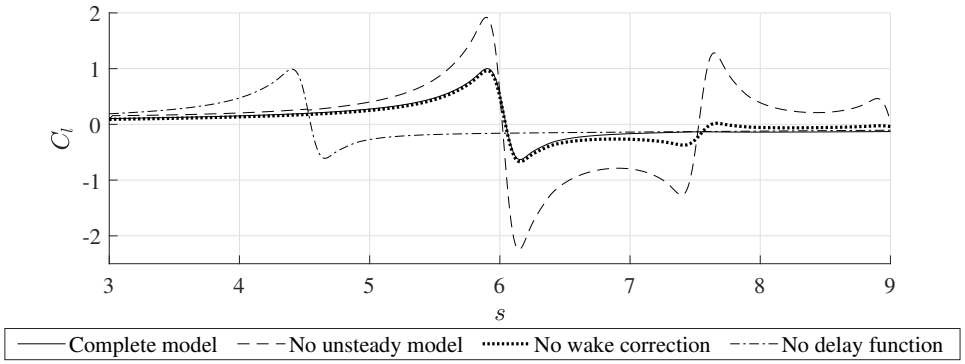

Fig. 16 Coefficient of lift during head-on BVI for a vortex with $r_c = 0.05c$ and $\Gamma = 0.4$.

In Fig. 17 the response of the unsteady aerodynamics model when coupled with the CFD solver is shown alongside the response of Beddoes' model with the input of the initial vortex profile. The responses to three different vortex core radii are shown ($r_c = 0.05c$, $0.1c$, and $0.2c$) each with two different circulations ($\Gamma = 0.2$, and 0.4). The agreement between the coupled and uncoupled models is excellent, further corroborating the validity of the coupling approach. The slight under-prediction of the coefficient of lift in the $r_c = 0.05c$ case is due to the dissipation of the vortex by the CFD solver as it is convected towards the airfoil.

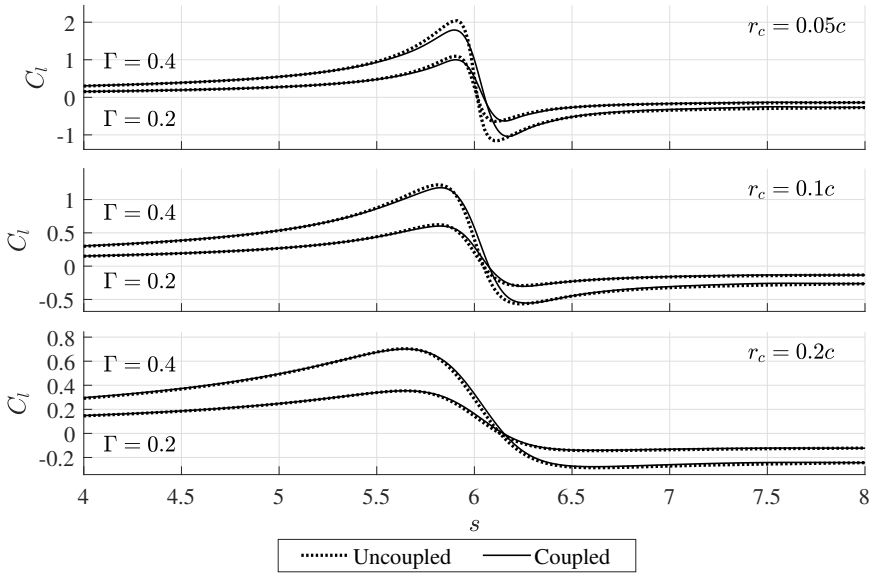

Fig. 17 Coefficient of lift during head-on BVI for a range of vortex strengths and core radii.

When the BVI is a near miss encounter the core radius is less significant to the velocity profile encountered by the airfoil. Because of this the coefficient of lift for a near miss BVI is shown only for the $r_c = 0.2c$ case in Fig. 18. The offset between the vortex and the airfoil is $0.26c$ in this case and the agreement between the uncoupled and coupled model is again excellent.

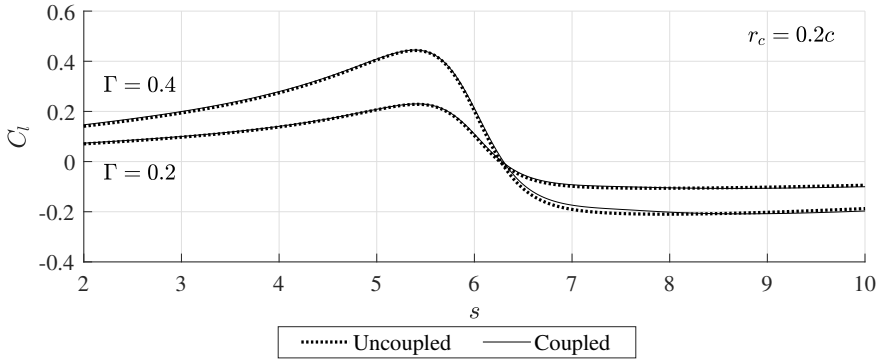

Fig. 18 Coefficient of lift during BVI with vertical separation of $\Delta y = 0.26c$.

Lastly, Fig. 19 shows contours of vorticity during a head-on encounter with a vortex with $r_c = 0.2c$ and $\Gamma = 0.4$. Figure 19 serves to illustrate the changes in the flow-field during the encounter. Typically, a head-on BVI will result in splitting of the vortex, possibly followed by dissipation and breakdown in the structure due to interaction with the viscous boundary layer. This loss of coherency and intensity causes head-on BVIs to be less severe than very near misses. In near misses the structure of the incident vortex is preserved and may induce the shedding of a more coherent

vortex from the airfoil, similar to that seen in a dynamic stall event. The momentum source method lacks the solid surface and the viscous boundary layer which cause the vortex splitting and breakdown that occurs in a head-on BVI, for this reason the flow-field in Fig. 19 more closely resembles that of a near-miss encounter with a large, coherent vortex being shed from the airfoil and forming a counter-rotating vortex pair with the incident vortex which is somewhat stretched by the encounter but largely preserves its vorticity.

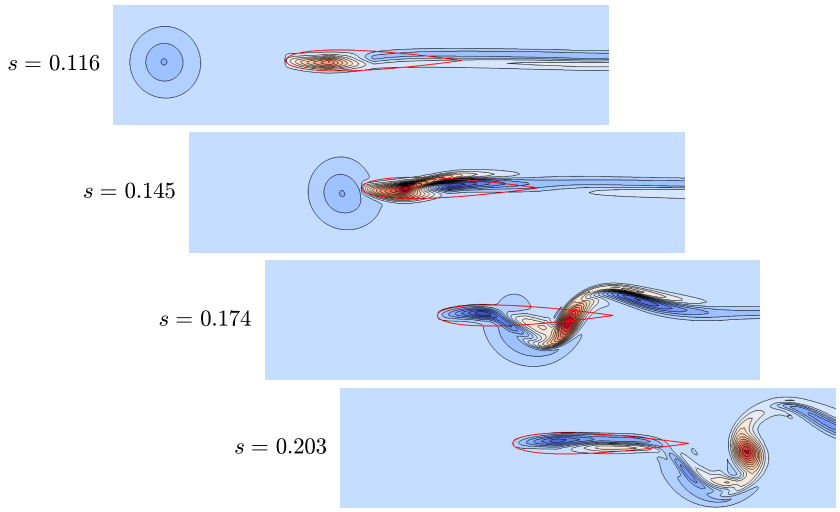

Fig. 19 Contours of vorticity during a head-on BVI event with $r_c = 0.2c$ and $\Gamma = 0.4$.

Steady-State Wing

The lift distributions from the resolved simulations and from the coupled simulations are compared in Fig. 20. The loading distribution from the coupled simulation is consistent with a lifting-line approximation and, relative to the resolved simulation, slightly underpredicts the lift towards the mid-span and overpredicts towards the tip. The use of a cosine distribution function for the spanwise points leads to points at the tip of the wing which are inside the core radius of the modelled tip vortex. The induced angle of attack for these points is thus much reduced, resulting in the spike in lift coefficient at the wing tip. The integrated coefficient of lift from the resolved simulation is 0.620 compared to 0.611 for the coupled simulation.

The resolved simulation (of 15 million points) reached convergence after approximately 10,000 iterations and 400 CPU hours while the coupled simulation (10 million points) reached convergence after 320 iterations and 20 CPU hours. Both simulations were run on 24 processors. The coupling method affords a significant decrease in simulation time, even accounting for differences in grid sizes between the cases presented here. When mesh generation time is also considered the time savings increase. In the coupled simulation the execution of the model accounted for 40% of the run time, though it should be noted that the lifting-line implementation is currently not parallelised.

The remaining analysis of the results of the steady-state wing simulations is focused on the development of the tip

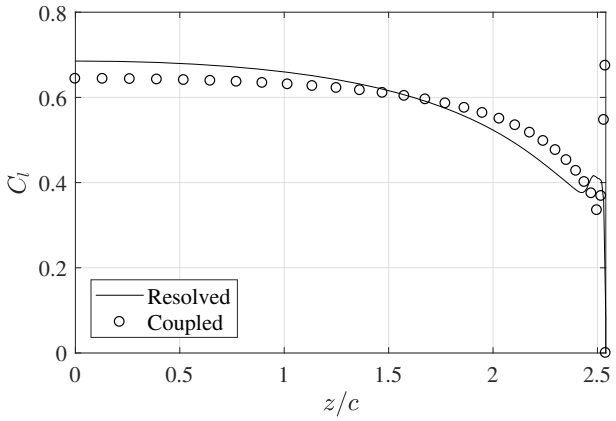

Fig. 20 Lift distribution from resolved CFD simulation and coupled simulation.

vortices as these are the defining feature of the wakes of both fixed and rotating wings. To function as a useful tool the momentum source representation must generate tip vortices similar to those formed in resolved simulations and observed in experiments. Figures 21 and 22 show contours of the spanwise velocity component and the streamwise vorticity component at the PIV sample planes in Figure 11. These figures show good agreement between the experimental and simulation data in terms of strength and position of the tip vortex. Both of the simulations exhibit similar dissipation of the vortex by $x_t/c = 2.0$ compared to the experimental data. The shape of the vortex in the coupled simulation immediately after formation ($x_t/c = 0.02$ and 0.5) is far more symmetric than the resolved or experimental vortices. However the tendency of the vortex to become symmetric leads to similar vortex shapes by the last sample plane.

A more quantitative comparison of the evolution of the tip vortices in the resolved and coupled simulations is shown in Figure 23. The vortex cores were extracted through eigen-analysis of the velocity field[28] and 32 equally spaced radial lines were drawn from these points on planes perpendicular to the vortex. The circumferential velocity (u_c) was then sampled along each of these lines and averaged around the circumference. The resulting mean velocity profiles are plotted at several streamwise locations in Figure 23. These profiles are very similar although the peak velocity of the vortex in the resolved simulation diminishes faster than the vortex in the coupled simulation and the core radius is larger.

The decay in peak velocity and increase in core radius are plotted as a function of streamwise position in Figure 24. The peak velocity initially decays faster in the resolved simulation, though both simulations converge to similar values. Both simulations show an approximately linear growth in vortex core size with the coupled simulation maintaining a tighter vortex. The fact that the resolved blade has a square tip geometry should be highlighted as different tip geometries may be employed to generate significantly different tip vortex structures[29] which the momentum source method presented here does not have the ability to capture.

The trajectories of the tip vortices (Figure 25) from both simulations remain closely aligned. At 60 chord lengths from the wing tip the vortex cores from the two simulations are separated by less than a quarter of a chord length.

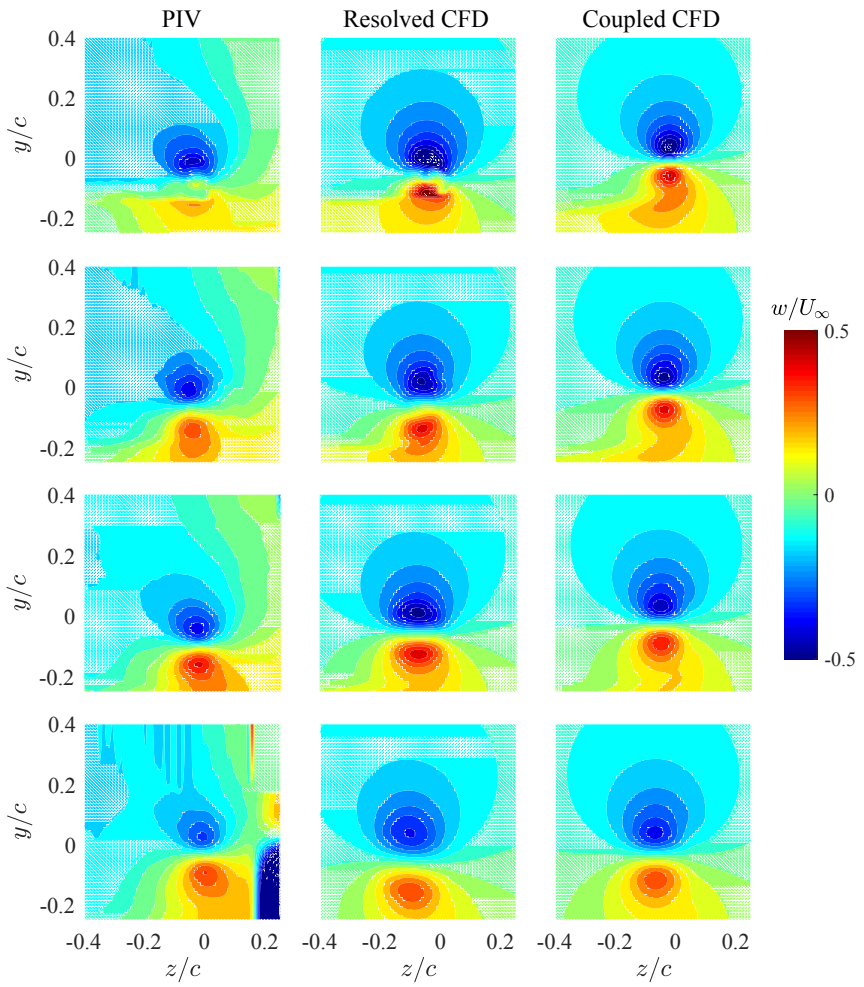

Fig. 21 Contours of z-component of velocity from PIV of Margaris and Gursul[27], resolved CFD simulation and coupled simulation. From top to bottom the sample planes are: $x_t/c = 0.02, 0.5, 1.0, 2.0$.

Conclusions

A method for producing two-way coupling between a simplified aerodynamics model and a CFD solver has been demonstrated. The key challenge is in extracting a meaningful incident velocity from the CFD flow-field. Sampling near the airfoil will give non-physical velocities due to the limitations of momentum source representations of lifting bodies (as illustrated in the case of the steady, 2D airfoil), while sampling away from the airfoil leads to challenges with unsteady aerodynamics. A delay function was introduced to correct for the time between the velocity being sampled and that velocity being incident at the airfoil. An additional model for the unsteady induced velocity at the sample point was also introduced. This model accounts for the impact of the shed vorticity in the wake of the airfoil. Together, these two developments remove any influence of the coupling in unsteady cases involving step changes in angle of attack, pitch oscillation, and BVI. This implies that these methods are suitable for extracting meaningful incident velocities from

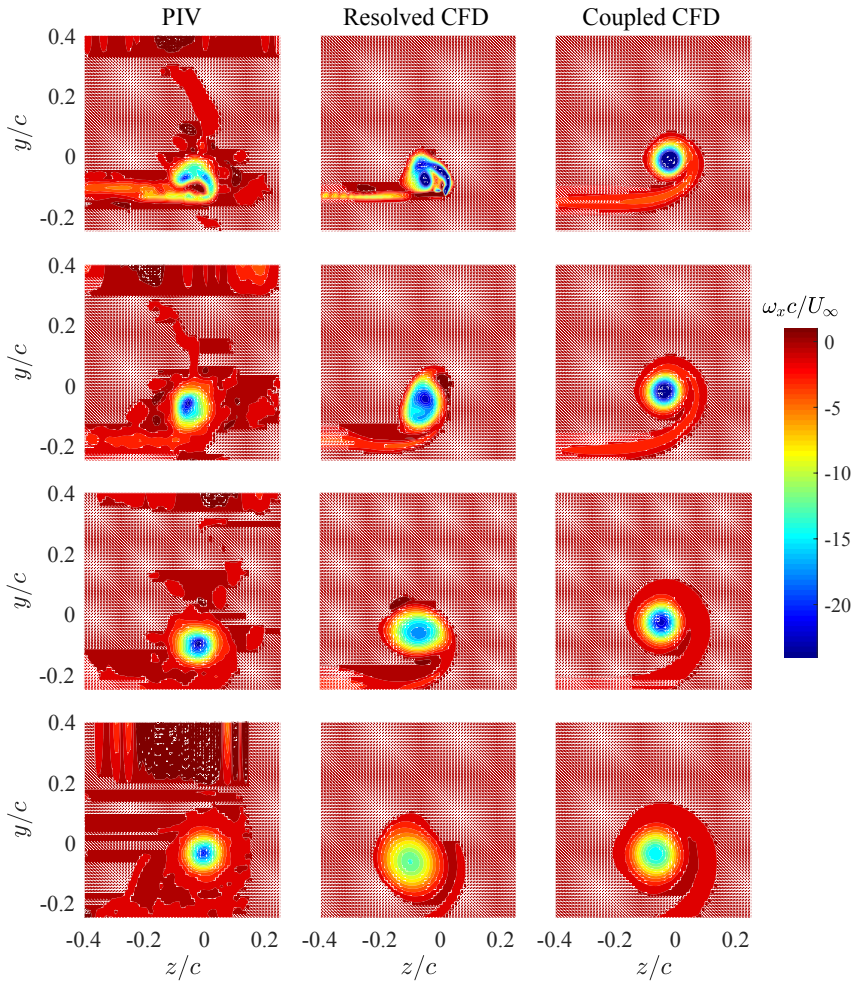

Fig. 22 Contours of vorticity from PIV of Margaris and Gursul[27], resolved CFD simulation and coupled simulation. From top to bottom the sample planes are: x_t/c = 0.02, 0.5, 1.0, 2.0.

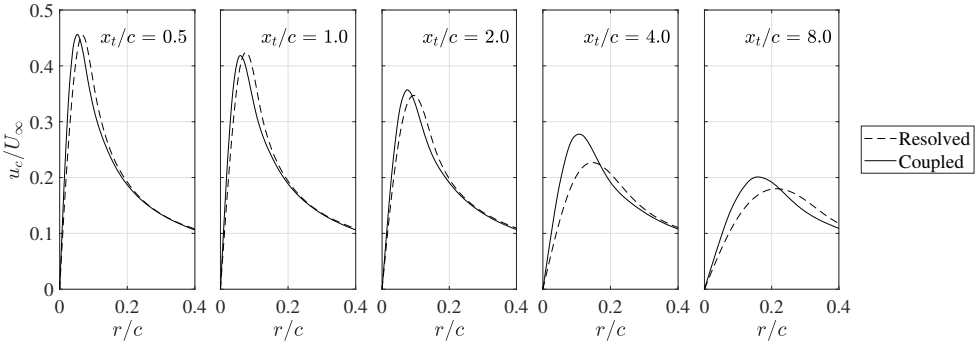

Fig. 23 Averaged circumferential velocity (u_c) profile across tip vortex from resolved CFD simulation and coupled simulation.

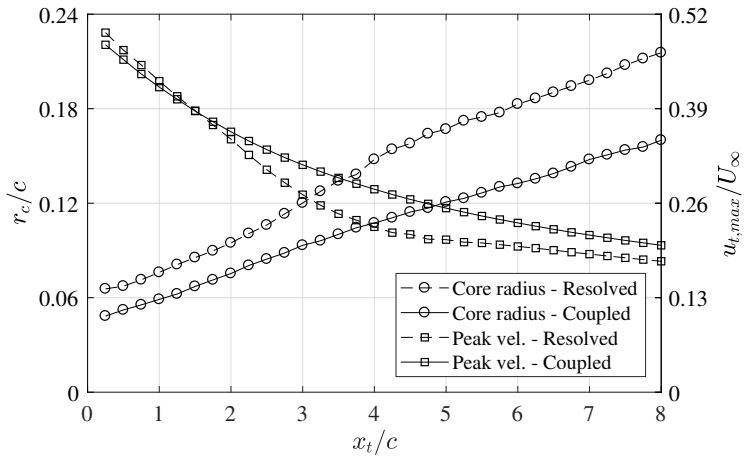

Fig. 24 Tip vortex radius (r_c/c) and peak circumferential velocity ($u_{t,max}/cU_\infty$) from resolved CFD simulation and coupled simulation.

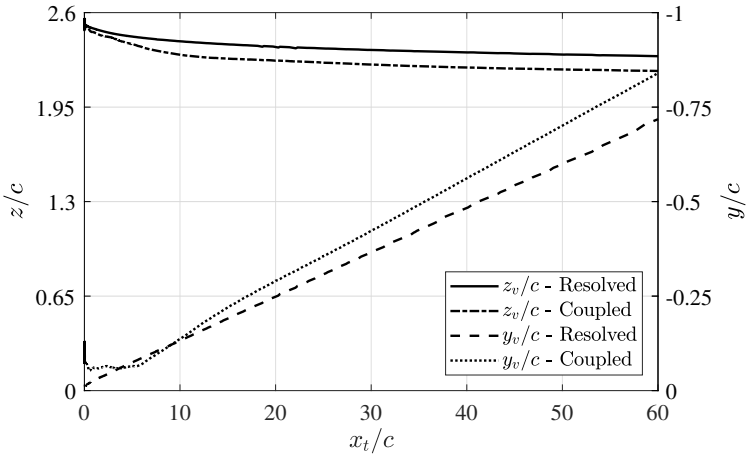

Fig. 25 Tip vortex trajectory from resolved CFD simulation and coupled simulation.

unsteady flow-fields.

The case of the finite aspect ratio wing in steady flow demonstrates the ability of momentum source methods to generate flow-fields of comparable fidelity to a resolved simulation in the mid- to far-field. In the near-wake of the 3D wing ($x_t/c < 1.0$) the asymmetry of the tip vortex is not captured, but this difference in shape rapidly disappears. Further downstream the tip vortex in the coupled simulation exhibits less spreading than that from the resolved simulation implying better preservation of the vortex than in the resolved case. Given the high resolution of both grids this difference is likely due to the higher turbulent eddy viscosity in the vortex core of the resolved case. This analysis of the wake leads us to conclude that the momentum source representation is capable of generating CFD wakes for isolated wings with accuracy comparable to those generated by resolved simulations in the mid- to far-wake.

Funding Sources

This research was funded by the Australian Defence Science and Technology Group.

Acknowledgments

The authors would like to thank the Australian Defence Science and Technology Group for providing funding and support for this work. The authors also acknowledge the University of Sydney HPC service at The University of Sydney for providing HPC resources that have contributed to the research results reported within this paper.

References

[1] Johnson, F., Tinoco, E., and Yu, J., "Thirty Years of Development and Application of CFD at Boeing Commercial Airplanes, Seattle," *Computers and Fluids*, Vol. 34, No. 10. doi:10.1016/j.compfluid.2004.06.005.

[2] Spalart, P., and Venkatakrishnan, V., "On the Role and Challenges of CFD in the Aerospace Industry," *The Aeronautical Journal*, Vol. 120, No. 1223. doi:10.1017/aer.2015.10.

[3] Steijl, R., and Barakos, G., "CFD Analysis of Complete Helicopter Configurations - Lessons learnt from the GOAHEAD Project," *Aerospace Science and Technology*, Vol. 19, No. 1. doi:10.1016/j.ast.2011.01.007.

[4] Hariharan, N., Narducci, R., Reed, E., and Egolf, A., "AIAA Standardized Hover Simulation: Hover Performance Prediction Status and Outstanding Issues," *55th AIAA Aerospace Sciences Meeting*, 2017. doi:10.2514/6.2017-1429.

[5] Conlisk, A., "Modern Helicopter Rotor Aerodynamics," *Progress in Aerospace Sciences*, Vol. 27, No. 5. doi:10.1016/s0376-0421(01)00011-2.

[6] Meyers, J., and Meneveau, C., "Optimal Turbine Spacing in Fully Developed Wind Farm Boundary Layers," *Wind Energy*, Vol. 15, No. 2. doi:10.1002/we.469.

[7] Chamorro, L., and Porte-Agel, F., "A Wind-Tunnel Investigation of Wind-Turbine Wakes: Boundary-Layer Turbulence Effects," *Boundary-Layer Meteorology*, Vol. 132, No. 1. doi:10.1007/s10546-009-9380-8.

[8] Forrest, J., Owen, I., Padfield, G., and Hodge, S., "Ship-Helicopter Operating Limits Prediction Using Piloted Flight Simulation and Time-Accurate Airwakes," *Journal of Aircraft*, Vol. 49, No. 4. doi:10.2514/1.c031525.

[9] Rajagopalan, R., and Mathur, S., "Three Dimensional Analysis of a Rotor in Forward Flight," *Journal of the American Helicopter Society*, Vol. 38, No. 3. doi:10.4050/jahs.38.14.

[10] Sorensen, J., and Shen, W., "Numerical Modeling of Wind Turbine Wakes," *Journal of Fluids Engineering*, Vol. 124, No. 2. doi:10.1115/1.1471361.

[11] Shen, W., Zhang, J., and Sorensen, J., "The Actuator Surface Model: A New Navier-Stokes Based Model for Rotor Computations," *Journal of Solar Energy Engineering*, Vol. 131, No. 1. doi:10.1115/1.3027502.

[12] Watters, C., and Masson, C., "Modeling of Lifting-Device Aerodynamics using the Actuator Surface Concept," *International Journal for Numerical Methods in Fluids*, Vol. 62, No. 11. doi:10.1002/fld.2064.

[13] Issa, R., "Solution of the Implicitly Discretised Fluid Flow Equations by Operator-Splitting," *Journal of Computational Physics*, Vol. 62, No. 1. doi:10.1016/0021-9991(86)90099-9.

[14] Van Doormaal, J., and Raithby, G., "Enhancements of the SIMPLE Method for Predicting Incompressible Fluid Flows," *Numerical Heat Transfer*, Vol. 7, No. 2. doi:10.1080/01495728408961817.

[15] Menter, F., "Two-Equation Eddy-Viscosity Turbulence Models for Engineering Applications," *AIAA Journal*, Vol. 32, No. 8. doi:10.2514/3.12149.

[16] van Leer, B., "Towards the Ultimate Conservative Difference Scheme. II. Monotonicity and Conservation combined in a Second-Order Scheme," *Journal of Computational Physics*, Vol. 14, No. 4. doi:10.1016/0021-9991(74)90019-9.

[17] Kim, T., Oh, S., and Yee, K., "Improved Actuator Surface Method for Wind Turbine Applications," *Renewable Energy*, Vol. 76. doi:10.1016/j.renene.2014.11.002.

[18] Jha, P., Churchfield, M., Moriarty, P., and Schmitz, S., "Guidelines for Volume Force Distributions Within Actuator Line Modeling of Wind Turbines on Large-Eddy Simulation-Type Grids," *Journal of Solar Engineering*, Vol. 136, No. 3. doi:10.1115/1.4026252.

[19] Shen, W., Hansen, M., and Sorensen, J., "Determination of Angle of Attack (AOA) for Rotating Blades," *Proceedings of the Euromech Colloquium - Wind Energy 2005*, 2005. doi:10.1007/978-3-540-33866-6_37.

[20] Beddoes, T., "Practical Computation of Unsteady Lift," *Vertica*, Vol. 8, No. 1.

[21] Lomax, H., Heaslet, M., Fuller, F., and Sluder, L., "Two- and Three-Dimensional Unsteady Lift Problems in High-Speed Flight," TR 1077, NACA, 1952.

[22] Jones, R., "Correction of the Lifting-Line Theory for the Effect of the Chord," TN 817, NACA, 1941.

[23] Lambourne, N., Zwaan, R., Davis, S., Landon, R., and Mabey, D., "Compendium of Unsteady Aerodynamic Measurements," Tech. rep., AGARD, 1982.

[24] Widnall, S., "Helicopter Noise due to Blade-Vortex Interaction," *Journal of the Acoustical Society of America*, Vol. 50, No. 10. doi:10.1121/1.1912640.

[25] Wilder, M., and D.P., T., "Parallel Blade-Vortex Interaction," *Journal of Fluids and Structures*, Vol. 12. doi:10.1006/jfls.1998.0172.

[26] Scully, M., "Computation of Helicopter Rotor Wake Geometry and its influence on Rotor Harmonic Airloads," Ph.D. thesis, Massachusetts Institute of Technology, 1975.

[27] Margaris, P., and Gursul, I., "Effect of Steady Blowing on Wing Tip Flowfield," *2nd AIAA Flow Control Conference*, 2004. doi:10.2514/6.2004-2619.

[28] Haimes, R., and Kenwright, D., "On the Velocity Gradient Tensor and Fluid Feature Extraction," *14th AIAA Computational Fluid Dynamics Conference*, 1999. doi:10.2514/6.1999-3288.

[29] Brocklehurst, A., and Barakos, G., "A Review of Helicopter Rotor Blade Tip Shapes," *Progress in Aerospace Sciences*, Vol. 56, No. 1. doi:10.1016/j.paerosci.2012.06.003.